High-resolution tomographic diffractive microscopy in reflection configuration

Guillaume Maire,[1,]* Yi Ruan,[1] Ting Zhang,[1] Patrick C. Chaumet,[1] Hugues Giovannini,[1] Daniel Sentenac,[3] Anne Talneau,[2] Kamal Belkebir,[1] and Anne Sentenac[1]

[1]*Aix Marseille Université, CNRS, Centrale Marseille, Institut Fresnel, UMR 7249, 13013 Marseille, France*
[2]*Lab Photon & Nanostruct, 91460 Marcoussis, France*
[3]*European Gravitational Observatory, 56021 Cascina (PI), Italy*
*Corresponding author: guillaume.maire@fresnel.fr

Tomographic diffractive microscopy (TDM) is a label-free imaging technique that reconstructs the 3D refractive index map of the probed object with an improved resolution compared to confocal microscopy. In this work, we consider a TDM implementation in which the sample is deposited on a reflective substrate. We show that this configuration requires calibration and inversion procedures that account for the presence of the substrate for getting highly resolved quantitative reconstructions. © 2013 Optical Society of America

OCIS codes: (180.6900) Three-dimensional microscopy; (110.6955) Tomographic imaging; (110.3200) Inverse scattering; (110.1758) Computational imaging.

http://dx.doi.org/10.1364/JOSAA.30.002133

1. INTRODUCTION

Tomographic diffractive microscopy (TDM) has recently emerged from digital holographic microscopy (DHM) as a powerful technique to reconstruct in 3D the map of relative permittivity of the probed sample with a high resolution [1]. Like DHM, it retrieves both the amplitude and the phase of the field scattered by the sample, classically from the interference pattern produced with a reference beam, in an on-axis arrangement or an off-axis one. Whereas in DHM the sample is illuminated at normal incidence only, TDM additionally requires to perform this detection successively for hundreds of different illumination angles, which permits to obtain a 3D reconstruction and increases the resolution. TDM is also known in the literature under other appellations, like synthetic aperture microscopy, phase tomography, or optical tomography. So far, this technique has been applied successfully for 3D samples mainly in the case of biological samples, where the permittivity contrast is weak and linear approximations (such as the Born approximation) can be used to calculate the scattered field [2–7]. In this case, the sample is reconstructed by applying a linear inversion algorithm to the set of data. The transverse resolution gain through the multi-illumination measurement can then be quantified by synthetic aperture generation: the equivalent numerical aperture (NA) of the system becomes equal to the sum of the NA used to collect the scattered field and the one defined by the illumination angle range [8]. Resolutions beyond the classical Rayleigh criterion have been obtained using this approach [1,3,6].

In most TDM implementations, the illumination and detection are operated from two opposite sides of the sample (transmission configuration) and the sample is assumed to be plunged in an homogeneous medium. This assumption is valid when imaging biological objects deposited on a coverslip and immersed in an index-match liquid. On the other hand, it does not hold when considering samples coming from the material science or the microelectronic domain, which are generally obtained on nontransparent substrates. Moreover, it has been shown theoretically [9] that the axial resolution of TDM could be significantly ameliorated if the samples were deposited on a highly reflecting substrate [9–11]. Hence, to ameliorate TDM performances and enlarge its application domain, it appears highly desirable to adapt the experimental mounting and the inversion procedures to the reflection configuration.

Up to now, TDM in reflection has been essentially used to recover qualitative two-dimensional (2D) super-resolved images of the sample reflectance [12–14], whereas our group used it to retrieve quantitative super-resolved 2D profiles of samples invariant along one of the transverse directions [15–17]. In a recent letter by our group [18], we have shown that, using an appropriate reconstruction procedure accounting for the presence of the substrate, TDM could yield the three-dimensional (3D) permittivity distribution of samples deposited on highly reflective substrates. In addition to providing 3D quantitative images, our iterative reconstruction approach permitted to decrease by a factor of 10 the number of illumination angles that are generally required for Fourier-based inversion algorithms [18], thus diminishing significantly the acquisition time. In this paper, we detail the experimental mounting, the calibration procedures and we describe different inversion methods adapted to reflection TDM. We test our system on well-controlled subwavelength resin nanostructures deposited on a silicon wafer.

The paper is structured as follows. Section 2 recalls the basics of TDM and compares the principles of the standard Fourier-based reconstruction procedure to that of our iterative inversion algorithm. In Section 3, the experimental setup

is described along with the normalization procedure that has to be applied to the data in order to get quantitative results. Last, Section 4 displays the reconstructions obtained with the Fourier-based algorithm and that obtained with the iterative procedure under various approximations.

2. BASICS OF TDM AND COMPARISON BETWEEN THE CONVENTIONAL FOURIER-BASED INVERSION PROCEDURE AND THE ITERATIVE NONLINEAR RECONSTRUCTION TECHNIQUE

Basically, TDM consists of recording the complex field $\mathbf{E}^s(\mathbf{k}, \mathbf{k}_l)$ that is scattered by the sample in the $\mathbf{k}$ direction when the illumination is a plane wave with $\mathbf{k}_l$ wave vector. This is done along M scattering directions $\mathbf{k}$ for L successive illuminations $\mathbf{k}_l$ accessible within the NA of the microscope objective. These data are processed with an inversion algorithm in order to get the 3D relative permittivity ε of the sample.

At the core of any TDM inversion method is the interaction model that links the scattered field $\mathbf{E}^s(\mathbf{k}, \mathbf{k}_l)$ to the sample permittivity contrast χ with $\chi = \varepsilon - 1$ if the sample is in air. From Maxwell equations, one shows that the scattered field, which is equal to the total macroscopic field $\mathbf{E}$ minus the reference field $\mathbf{E}^{\text{ref}}$ that would exist in absence of the sample, verifies

$$\mathbf{E}^s(\mathbf{k}, \mathbf{k}_l) = \int_V \mathbf{g}(\mathbf{k}, \mathbf{r}') \chi(\mathbf{r}') \mathbf{E}(\mathbf{r}', \mathbf{k}_l) d\mathbf{r}', \qquad (1)$$

where V is the sample support and $\mathbf{g}$ is the far-field Green tensor, $\mathbf{g}(\mathbf{k}, \mathbf{r}')\mathbf{p}$ is the far field emitted in the $\mathbf{k}$ direction by a dipole $\mathbf{p}$ placed at $\mathbf{r}'$ in the reference medium (which is defined as the geometry without the sample). In general, the total field $\mathbf{E}$ depends on χ so that the relationship between $\mathbf{E}^s$ and χ is nonlinear.

A. Fourier-Based Inversion Method
To reconstruct the sample, most TDM inversion procedures are based on a linearized approximation of Eq. (1), the Born approximation, which is obtained by assuming that the field inside the probed object is close to the reference field. It is valid for small and weakly contrasted samples, ($\chi \ll 1$). Moreover, the vectorial nature of the recorded field is usually overlooked and the reference medium is assumed to be homogeneous. With this scalar approach, the far-field Green tensor can be assimilated to a simple Fourier operator, $g(\mathbf{k}, \mathbf{r}')p \propto \exp(-i\mathbf{k} \cdot \mathbf{r}')p$ [1,3–6,8,14,19], and the reference field to a simple plane wave, $E^{\text{ref}}(\mathbf{r}, \mathbf{k}_l) \propto \exp(i\mathbf{k}_l \cdot \mathbf{r})$. As a consequence, the scattered field can be written as

$$E^s(\mathbf{k}, \mathbf{k}_l) \propto \tilde{\chi}(\mathbf{k} - \mathbf{k}_l), \qquad (2)$$

where $\tilde{\chi}$ is the 3D Fourier transform of χ. Hence, for a given illumination angle and for all the $\mathbf{k}$ wave vectors allowed by the NA used for the detection, the scattered far field gives access to the Fourier components of the permittivity contrast on a cap of sphere centered on the extremity of vector $-\mathbf{k}_l$ [19,20]. Changing the illumination angle permits to shift this cap of sphere in the Fourier space and measure different Fourier components. Therefore, merging the data collected

for various angles enlarges the accessible Fourier domain. This synthetic aperture generation enables a 3D reconstruction of the object and ameliorates the resolution compared to images obtained with classical confocal microscopy. In practice, the measured scattered fields for a given $\mathbf{k} - \mathbf{k}_l$ are added and averaged for reducing the experimental noise. Note that extracting the scattered field from the measured total field for $\mathbf{k} - \mathbf{k}_l \approx 0$ is usually not possible in the standard experimental configuration as the scattered signal is overwhelmed by the reference field. Then, the object can be reconstructed in 3D by simply applying a 3D inverse Fourier transform to the whole dataset. However, this approach typically requires hundreds of illuminations to fill the whole accessible Fourier domain with fine enough discretization steps for the Fourier transform to be accurate.

B. Nonlinear Iterative Inversion
To ameliorate the reconstruction procedure, we have developed an inversion method based on a rigorous vectorial modeling of the field scattered by the object [18,21–24]. Our approach does not assume that the field inside the sample is close to the incident field and is adapted to a reference medium with a reflecting substrate.

1. Formulation of the Forward Scattering Problem
The scattered far field satisfies Eq. (1) with a far-field Green tensor that accounts for the interface [21]. To calculate the total field inside the sample, one uses the self-consistent integral equation [23],

$$\mathbf{E}(\mathbf{r}) = \mathbf{E}^{\text{ref}}(\mathbf{r}) + \int_V \mathbf{G}(\mathbf{r}, \mathbf{r}') \chi(\mathbf{r}') \mathbf{E}(\mathbf{r}') d\mathbf{r}', \qquad (3)$$

where $\mathbf{G}(\mathbf{r}, \mathbf{r}')\mathbf{p}$ is the electric field at $\mathbf{r}$ emitted by a dipole placed at $\mathbf{r}'$ in the reference medium. When both $\mathbf{r}$ and $\mathbf{r}'$ are above the substrate, it corresponds to the sum of the free-space radiated field [25] and of the substrate reflected field (which is computed *via* a quadrature [26]). The reference field is also the sum of the incoming plane wave and its reflected outgoing counterpart. Equation (3) can be solved numerically using an appropriated discretization [23].

2. Formulation of the Inverse Scattering Problem
The iterative inversion procedure consists of retrieving simultaneously the sample permittivity contrast χ and the total field $\mathbf{E}_l$ in a bounded investigation domain Ω (outside Ω, χ is assumed to be null) from the set of scattered field data $\mathbf{f}_l$ recorded on the far-field surface Γ for $l = 1, \dots, L$ incident directions. In most of the following examples, Ω is located above the substrate and its lower boundary lays at the air–substrate interface. Starting from an initial guess, χ and $\mathbf{E}_l$ are gradually adjusted so as to minimize some cost functional involving the measured data. For the sake of simplicity, symbolic notation is introduced for describing the far-field and self-consistent near-field integral equations,

$$\mathbf{E}_l^s = \underline{\underline{B}} \chi \mathbf{E}_l, \qquad (4)$$

$$\mathbf{E}_l = \mathbf{E}_l^{\text{ref}} + \underline{\underline{A}} \chi \mathbf{E}_l. \qquad (5)$$

In Eq. (4), the volume integral is performed over Ω and numerically solved by discretizing Ω into N subunits on a cubic lattice with period much smaller than the wavelength of illumination. The operator $\underline{\underline{B}}$ is a $3N \times 3M$ matrix including the nine components of the far-field Green tensor for each $\mathbf{r}$ in Ω and each $\mathbf{k}$ on Γ. The operator $\underline{\underline{A}}$ is a $3N \times 3N$ matrix including the nine components of the near-field Green tensor for each $\mathbf{r}$ and $\mathbf{r}'$ in Ω. It is worth noting at this point that solving the self-consistent near-field equation is time consuming and may be impossible for large Ω.

For the present work we have used a cost functional that reads (for iteration number n)

$$\mathcal{F}_n(\chi_n, \mathbf{E}_{l,n}) = \frac{\sum_{l=1}^{L} \|\mathbf{h}_{l,n}^{(1)}\|_\Gamma^2}{\sum_{l=1}^{L} \|\mathbf{f}_l\|_\Gamma^2} + \frac{\sum_{l=1}^{L} \|\mathbf{h}_{l,n}^{(2)}\|_\Omega^2}{\sum_{l=1}^{L} \|\mathbf{E}_l^{\mathrm{ref}}\|_\Omega^2} \qquad (6)$$

$$= W_\Gamma \sum_{l=1}^{L} \|\mathbf{h}_{l,n}^{(1)}\|_\Gamma^2 + W_\Omega \sum_{l=1}^{L} \|\mathbf{h}_{l,n}^{(2)}\|_\Omega^2, \qquad (7)$$

where W_Γ and W_Ω are normalization coefficients, and $\mathbf{h}_{l,n}^{(1)}$ and $\mathbf{h}_{l,n}^{(2)}$ are two residual errors for Eqs. (4) and (5), respectively:

$$\mathbf{h}_{l,n}^{(1)} = \mathbf{f}_l - \underline{\underline{B}} \chi_n \mathbf{E}_{l,n}, \qquad (8)$$

$$\mathbf{h}_{l,n}^{(2)} = \mathbf{E}_l^{\mathrm{ref}} - \mathbf{E}_{l,n} + \underline{\underline{A}} \chi_n \mathbf{E}_{l,n}. \qquad (9)$$

The minimization is performed with the hybrid gradient procedure described in [24], which requires to solve one forward problem at each iteration. The two sequences χ and $\mathbf{E}_l$ are initiated by applying the complex conjugate transposed matrix $\underline{\underline{B}}$ to the dataset $\mathbf{f}_l$ [26].

3. EXPERIMENTAL SETUP AND PROCEDURE

A. Setup Architecture
We have developed a TDM setup based on a synthetic aperture digital microscope working in reflection, presented in Fig. 1 [27]. The linearly polarized light emitted at 633 nm by a 10 mW helium–neon laser is divided into a reference beam, passing through an electro-optic phase modulator (PM), and a beam directed toward the sample. A rotating mirror (M) permits to control the deflection of this latter beam, while a beam expander (BE) and diaphragm (D) generate a wide collimated beam with near-homogeneous power density. This beam illuminates the sample after transmission through the microscope objective (OL) and the associated tube lens (L_1). It can be locally assimilated to a plane wave since the dimensions of the object are small compared to the width of the beam. The center of the mirror is conjugated with the center of the sample through the BE, the tube lens, and the microscope objective. Thus, rotating the mirror varies the incidence angle without shifting laterally the illumination beam on the object. The polar angle of the illumination can be varied over the whole NA of the objective. The field scattered by the object is collected by the microscope objective (Zeiss Epiplan-Apochromat $50\times$, NA = 0.95) and imaged on a CCD camera (Kappa PS4-1020) after passing through relay lenses L_2 and L_3 to
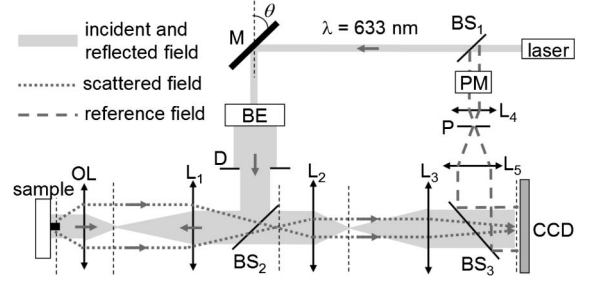

Fig. 1. Sketch of the experimental setup: M, rotating mirror; BE, beam expander; D, diaphragm; OL, objective lens; L_1, tube lens; $L_{2,...,5}$, lenses; $BS_{1,...,3}$, beam splitters; PM, phase modulator; P, pinhole.

obtain a global magnification of about 290. This provides a very high sampling of 26 nm per pixel, that easily satisfies the Shannon criterion even at half the Abbe limit (the Abbe limit is here $0.5\lambda/\mathrm{NA} = 333$ nm). After spatial filtering with a pinhole (P) and collimation, the reference field is coherently superimposed on the image field thanks to beam splitter BS_3.

For each illumination l, the amplitude and phase of the image field $\mathbf{E}_l^{\mathrm{im}}$ are retrieved by phase-shifting interferometry. $\mathbf{E}_l^{\mathrm{im}}$ is detected on a plane conjugated with the microscope object focal plane. Now, our nonlinear inversion procedure requires the scattered far-field $\mathbf{f}_l$ for all possible $\mathbf{k} \in \Gamma$. Thus, the measurements $\mathbf{E}_l^{\mathrm{im}}$ have to be transferred numerically to the far field with a 2D discrete inverse Fourier transform. The directions of $\mathbf{k}$ that are close to the specular reflection on the silicon substrate are discarded, since the field scattered by the object is there masked by the specular reflection. Note that what is effectively measured at the image plane is a projection of the vectorial image field on the polarization state of the reference beam, which is that of the illumination beam. Thus, the minimization of Eq. (8) is performed for the projection of the far field on this polarization state only.

B. Normalization Procedure of the Measurements
To retrieve a quantitative 3D permittivity map of the sample, it is necessary to apply a normalization procedure to the amplitude and the phase of the measured scattered field prior to performing the inversion. The normalization is necessary to correct the laser intensity fluctuations and the optical path variation between the reference and illumination beams that possibly occur when changing the illumination angle. In classical TDM in free-space under Born approximation configuration, the global relative phase and amplitude of the scattered field $\mathbf{f}_l$ under illumination l are set to match the measurements obtained at illumination $l-1$ by comparing the far-field complex amplitudes obtained along the directions $\mathbf{k}, \mathbf{k}'$, such that $(\mathbf{k}' - \mathbf{k}_{l-1}) = (\mathbf{k} - \mathbf{k}_l)$, i.e., the same spatial frequency in Eq. (2) for two successive incidences. In our specific configuration with a reflecting substrate, there is no more overlapping domains in the Fourier space for comparing the data. The latter are normalized so that the specular reflection on the substrate matches, at each illumination (both in amplitude and phase), the theoretical specular reflection calculated by the forward scattering model. This implies that the specular reflection has to be far stronger than the field scattered in the same direction by the sample, which is verified for small objects.

1. Amplitude Normalization

The nonlinear inversion assumes that the object is illuminated for each angle of incidence by a plane wave with unity amplitude. The measured amplitudes $\|\mathbf{f}_l\|$ have therefore to be normalized according to this hypothesis so that a correct estimation of the permittivity can be retrieved. It is performed for each illumination l by multiplying $\mathbf{f}_l$ by the factor M_l:

$$M_l = \frac{|\gamma_l| r_l S}{2\pi \langle \|\mathbf{E}_l^{\text{im}}\| \rangle_S}, \qquad (10)$$

where γ_l is the projection of the incident wave vector on the optical axis of the microscope, r_l the modulus of the substrate Fresnel reflection coefficient for the incident polarization state, S the surface of the field of view that can be imaged on the CCD sensor. $\langle \|\mathbf{E}_l^{\text{im}}\| \rangle_S$ is the mean field modulus averaged over the field of view: as the object is small on the CCD image, it can be considered as the mean field modulus reflected by the substrate. The multiplication by M_l ensures that the maximal value of $\mathbf{f}_l$ in the far field, which corresponds to the specular reflection, is equal to that scattered by a portion of substrate of surface S when illuminated by a plane wave with unity amplitude, as calculated by the forward scattering model.

Note that once the factors M_l have been calculated, the digital holograms $\mathbf{E}_l^{\text{im}}$ are multiplied by a filter function to get rid of the field out of the region of interest containing the sample. This further diminishes the speckle noise that is already greatly reduced by the multi-illumination measurement.

2. Phase Normalization

In the forward model and the inverse procedure, the phase origin is placed on the air–substrate interface and in the middle of the transverse dimensions of the investigation domain Ω. Now, the scattered far-field $\mathbf{f}_l$ is obtained by 2D Fourier transforming the image field $\mathbf{E}_l^{\text{im}}$ recorded at the image plane. The transverse position of the phase origin (in the image plane) can be chosen visually at the center of the sample while its axial position is that of the image plane. The latter is generally not perfectly conjugated to the air–substrate interface. Calling $\mathbf{d} = d_z \hat{\mathbf{z}}$ the position of the plane conjugated with the image plane with respect to the air–substrate interface, the experimental phase $\varphi_s(\mathbf{k}, \mathbf{k}_l)$ of the scattered far field measured along direction $\mathbf{k}$ for the incident wave vector $\mathbf{k}_l$ is linked to the phase $\varphi_0(\mathbf{k}, \mathbf{k}_l)$ of the scattered far field obtained when the image plane and the air–substrate interface are perfectly conjugated by

$$\varphi_s(\mathbf{k}, \mathbf{k}_l) = \varphi_0(\mathbf{k}, \mathbf{k}_l) + (\mathbf{k} - \mathbf{k}_l) \cdot \mathbf{d}. \qquad (11)$$

The following section describes two methods enabling to retrieve d_z. Once d_z is determined, the scattered far-field phase is corrected for each observation and illumination directions using Eq. (11). Then, all the scattered phases $\varphi_s(., \mathbf{k}_l)$ obtained for a given illumination $\mathbf{k}_l$ are shifted by a constant so that the recorded phase in the specular reflected direction matches that of the theoretical Fresnel reflection coefficient (calculated with a phase origin laying on the air–substrate interface). This procedure ensures that the phase origin of the incident and scattered field corresponds to that chosen for the forward model.

C. Determination of the Phase Origin

To retrieve the axial position of the sample plane with respect to the image plane, d_z, one applies a 3D inverse Fourier transform (FT^{-1}) to the dataset $\mathbf{f}_l$ to get a rough estimation of the object. Prior the Fourier transform, the data are normalized as if d_z was equal to 0. The sample plane being usually close to the image plane (the interdistance remaining smaller than one wavelength thanks to the high NA of the objective), the reconstruction, although strongly distorted, is generally accurate enough to pinpoint an approximate sample center. The distance of the latter to the center of the reconstruction domain gives a first estimation of $\mathbf{d}$. The Fourier transform is then applied to the data normalized with the previously estimated $\mathbf{d}$. After a few iterations, the reconstruction is improved and d_z is better estimated.

Another technique, inspired by that described in [28], has also been developed. We call $\mathbf{f}_l'$ the dataset for which d_z has been corrected,

$$\mathbf{f}_l' = \mathbf{f}_l \exp(-i[\gamma - \gamma_l]d_z), \qquad (12)$$

where γ is the projection of $\mathbf{k}$ on the optical axis. The problem is stated as finding d_z so that the backpropagation [26] of the associated scattered field $\mathbf{f}_l'$ provides the best initial guess for the inversion scheme. This is accomplished by minimizing the cost function $\mathcal{G}$,

$$\mathcal{G} = \sum_{l=1}^{L} \|\mathbf{f}_l' - \beta \underline{\underline{B}}(\underline{\underline{B}}^\dagger \mathbf{f}_l')\|_{\Gamma}^2, \qquad (13)$$

where β is a complex scalar weight and $\underline{\underline{B}}^\dagger$ the complex conjugate transpose of matrix $\underline{\underline{B}}$. This second approach is more precise than the first one to estimate d_z, but it is more time consuming, especially for large investigation domains due to the two matrix vector products with $\underline{\underline{B}}$ in Eq. (13).

4. EXPERIMENTAL RESULTS ON OBJECTS AT THE RAYLEIGH LIMIT

To illustrate the performances of our inversion approach, we have imaged subwavelength resin objects deposited on a silicon substrate. The test sample consists of four identical resin cylinders centered at the corners of a square of side 400 nm, see Fig. 2. Note that 400 nm corresponds exactly to the Rayleigh limit of our microscope ($0.6\lambda/\text{NA} = 400$ nm). The diameter and height of the cylinders are 200 and 150 nm, respectively, and the relative permittivity of the resin at 633 nm is about 2. The dataset is obtained by illuminating the sample with 20 incident directions, 10 belonging to the plane of incidence (x, z) and 10 to the plane (y, z),
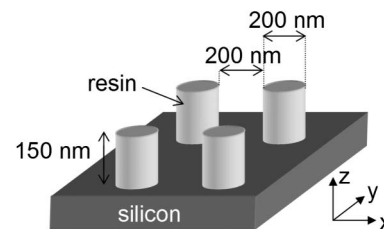

Fig. 2. Test sample: subwavelength resin cylinders deposited on a silicon substrate.

see Fig. 2. For each plane of incidence, the polar angles range from [−55° to 55°]. The linear polarization of the illumination beam remains in the (x, z) plane for all incident angles.

In this section, different inversion procedures are applied to the normalized set of data. Hereafter, for a fair comparison, we display the cuts of the different 3D reconstructions on the axial (x, z), (y, z) and transverse (x, y) planes containing the pixel of highest value.

A. Comparison of the Reconstructions Obtained with the Linear Inversion (3D FT^{-1}) and the Nonlinear Iterative Inversion

We first use the classical linear reconstruction procedure that consists of applying a 3D FT^{-1} to the dataset appropriately placed in the Fourier space, see Fig. 3. The discretization of the reconstruction is 53 nm and only the central part of the reconstruction is shown. We observe that, in the transverse plane, the four cylinders are hardly distinguishable and are surrounded by strong artefacts while, in the longitudinal plane, the axial profile of the cylinders is strongly distorted. This poor reconstruction can be explained by the numerous missing points in the Fourier space (to fill correctly the Fourier space, several hundreds of illumination would be required) and by the presence of the substrate, which is interpreted by the linear inversion as a mirror object, symmetrically placed below the substrate, that mingles with the original one.

We now turn to the "rigorous" iterative reconstruction technique described in Section 2. Prior to launching the inversion, the size of the investigation domain Ω where the unknown object will be reconstructed has to be determined. The transverse dimensions of the domain can be easily inferred from the image of the object on the camera. For its axial dimension, a starting value can be obtained from the distorted reconstruction given by the 3D FT^{-1} inversion. Alternatively, it can also be evaluated from the defocus of the image when the object is translated along the optical axis (the depth of field of the objective is about 1 μm at $\lambda = 633$ nm). We use the *a priori* information that the sample is deposited on a substrate so that the lowest boundary of Ω coincides with the air–substrate interface. The discretization step of Ω is taken equal to 50 nm.

The first reconstruction is performed with a relatively high and large investigation domain, see Fig. 4, then the size of Ω is decreased, while keeping the same discretization, to increase the data to unknowns ratio and improve the quality of the reconstruction, see Fig. 5. One can see that the four cylinders are perfectly resolved, with a good estimation of their width,
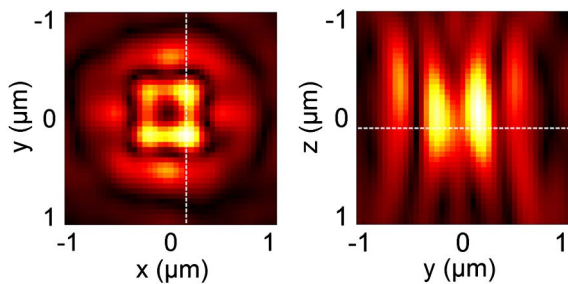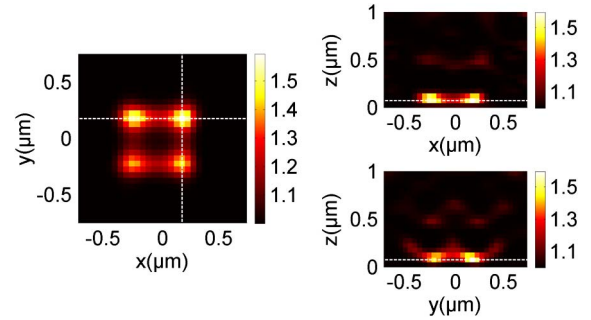

Fig. 4. Transverse cut (left) and longitudinal cuts (top and bottom) of the 3D permittivity map reconstructed with the nonlinear iterative inversion in a quite large domain. Cuts are along the white dashed lines.

height, spacing distance, and relative permittivity. The slight asymmetry of the reconstructions is due to residual speckle noise and experimental uncertainties on the realization and evaluation of the angular scanning. With the iterative inversion method, twenty illuminations are sufficient to get an accurate artefact-free image of the sample. We have checked on several other samples that it provides an isotropic resolution at the Rayleigh limit in the (x, y) plane.

B. Influence of the Substrate in the Nonlinear Iterative Inversion

The significant amelioration brought about by the nonlinear iterative inversion as compared to the classical 3D FT^{-1} linear approach stems from several reasons. First, it constrains the sample to be included in a given investigation domain which permits to fill the eventual missing points in the Fourier space. Then, it does not assume the Born approximation and performs a rigorous calculation of the scattered field, which accounts for the substrate following Eqs. (4) and (5). The price to pay for this rigorous modeling lays in the computation effort, which is particularly important for calculating the matrix $\underline{A}$ in the presence of the substrate and solve Eq. (5) for each iteration in the inversion procedure. As illustration, the reconstructions of Figs. 4 and 5 were obtained after 10 iterations, respectively in 90 min with 10 GB of RAM memory, and 25 min with 5 GB of RAM memory, on a computer with a standard processor.

It is therefore useful to perform the nonlinear iterative inversion with approximate calculations of the scattered field, both to get more physical insight into the origin of the reconstruction improvement and to accelerate the procedure.

1. Inversion Assuming No Substrate

We start with the most severe approximation: the presence of the substrate is ignored for calculating $\mathbf{E}^{\text{ref}}$, $\underline{A}$ and $\underline{B}$, as if the

Fig. 3. Transverse cut (left) and longitudinal cut (right) of the modulus of the 3D FT^{-1} of the dataset. Cuts are along the white dashed lines.
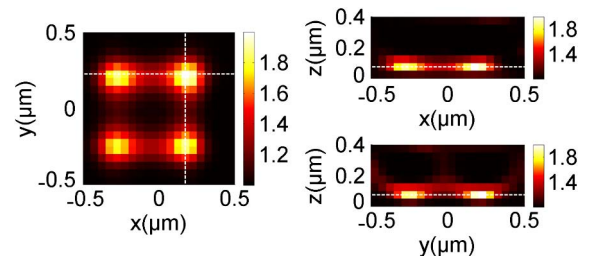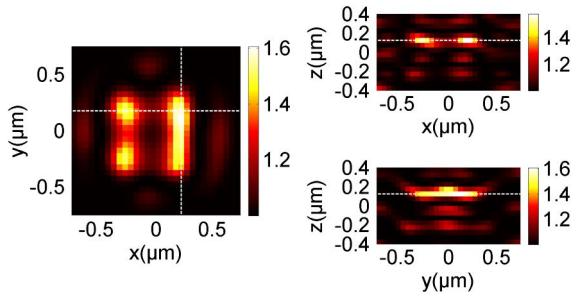

Fig. 5. Same as Fig. 4 with a tightened domain.

Fig. 6.   3D permittivity map assuming the sample is surrounded by air (no substrate), with an investigation domain symmetrical with respect to the substrate plane ($z = 0$).

sample was surrounded by air, like in the 3D FT^{-1} approach. In this case, the investigation domain Ω is taken symmetrical with respect to the substrate plane (the plane at $z = 0$), to get a configuration similar to the 3D FT^{-1} linear inversion. We observe in Fig. 6 that the reconstruction, while better than that of the FT^{-1} approach, is strongly deteriorated as compared to the rigorous inversion of Figs. 4 and 5. The four cylinders are not resolved and artefacts pollute the image. Mirror images of the cylinders can be seen symmetrically to the substrate plane, but they have a much smaller permittivity as the silicon substrate does not act as a perfect mirror. We have checked that if Ω is taken just above the substrate, the reconstruction is even more degraded.

2. Inversion Taking into Account the Substrate for E^{ref}
A first improvement is to calculate $\mathbf{E}^{ref}$ by taking the substrate into account. This means that the object is illuminated by the coherent superposition of the incident plane wave and its specular reflection on the substrate. This straightforward calculation is done without any computational effort in the algorithm. The corresponding object reconstruction is shown in Fig. 7. There are now far fewer artefacts and the four cylinders are almost resolved. This improvement can easily be explained by noting that the field scattered by an object above a mirror illuminated by a plane wave can be approximated by the field scattered by two objects in the air, symmetrically placed with respect to the mirror plane and illuminated by two symmetrical coherent plane waves. Nevertheless, when looking at the reconstruction into more details, the spacing distance between the cylinders is not accurately retrieved on the transverse cut of Fig. 7: it reaches 500 nm instead of 400 nm. Moreover, one can see on the bottom longitudinal cut of Fig. 7 that the two cylinders are not perfectly separated.
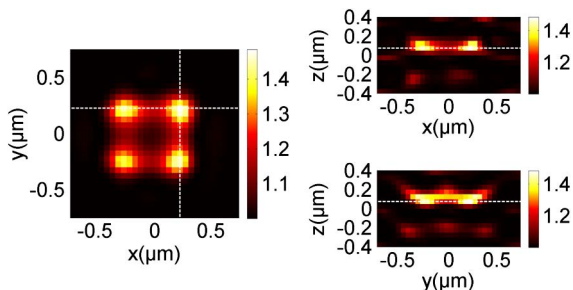

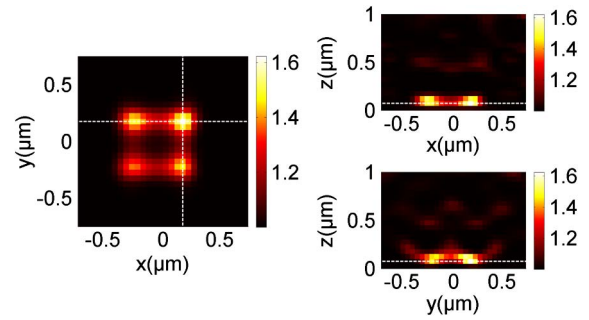Fig. 7.   Same as Fig. 6 when the substrate is taken into account for $\mathbf{E}^{ref}$ only.

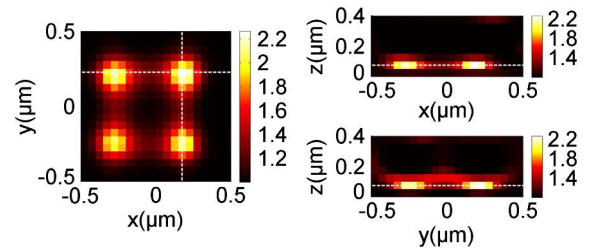Fig. 8.   Same as Fig. 4 when the substrate is taken into account for $\mathbf{E}^{ref}$ and $\underline{\underline{B}}$ only.

Fig. 9.   Same as Fig. 5 when the substrate is taken into account for $\mathbf{E}^{ref}$ and $\underline{\underline{B}}$ only.

We have again checked that taking Ω just above the substrate further deteriorates the reconstruction.

3. Inversion Taking into Account the Substrate for E^{ref} and $\underline{\underline{B}}$
A further improvement consists of taking the substrate into account also for calculating the far-field Green tensor $\underline{\underline{B}}$. This operation is not time consuming as there exists an analytical expression for the far-field operator [26]. In this case, the only approximation concerns the near-field operator $\underline{A}$, which is calculated in free-space. Note that the investigation domain is now again placed above the air–substrate interface.

We observe in Figs. 8 and 9 that the reconstruction is very close to that obtained with the rigorous inversion (Figs. 4 and 5). The main difference concerns the relative permittivity value, which is slightly overestimated when $\underline{A}$ does not take into account the interface. Such a behavior has also been observed on synthetic data in previous works [26]. It shows that the influence of the interface in the estimation of the total field inside the sample can be neglected in first approximation. Now, in free-space the susceptibility tensors of matrix $\underline{A}$ are analytical and yield a Toeplitz structure. This property permits to speed up significantly the resolution of Eq. (5).

5. CONCLUSION

In this paper, we have described the implementation of a tomographic diffractive microscope able to get 3D quantitative highly resolved images of samples deposited on an opaque substrate. We have proposed a specific phase and amplitude normalization of the data that ensures that the recorded scattered far field match the simulations. Then, we have studied the performance of a nonlinear iterative inversion method based on various approximations of the forward model (with or without substrate). We have shown that accounting for the substrate is primarily important in the calculation of the

illuminating field and of the far-field Green tensor. Finally, we have demonstrated experimentally that our TDM setup is able to retrieve the 3D quantitative permittivity distribution of subwavelength transparent objects deposited on silicon using only 20 different illumination angles. This achievement opens new fields of application for TDM and paves the way toward mirror-assisted isotropic resolution [9].

ACKNOWLEDGMENT

REFERENCES AND NOTES

1. V. Lauer, "New approach to optical diffraction tomography yielding a vector equation of diffraction tomography and a novel tomographic microscope," J. Microsc. **205**, 165–176 (2002).
2. Y. Sung, W. Choi, C. Fang-Yen, K. B. zadegan, R. R. Dasari, and M. S. Feld, "Optical diffraction tomography for high resolution live cell imaging," Opt. Express **17**, 266–277 (2009).
3. B. Simon, M. Debailleul, A. Beghin, Y. Tourneur, and O. Haeberlé, "High-resolution tomographic diffractive microscopy of biological samples," J. Biophotonics **3**, 462–467 (2010).
4. M. Kim, Y. Choi, C. Fang-Yen, Y. Sung, R. R. Dasari, M. S. Feld, and W. Choi, "High-speed synthetic aperture microscopy for live cell imaging," Opt. Lett. **36**, 148–150 (2011).
5. M. Mir, S. D. Babacan, M. Bednarz, M. N. Do, I. Golding, and G. Popescu, "Visualizing Escherichia coli sub-cellular structure using sparse deconvolution spatial light interference tomography," PLoS ONE **7**, e39816 (2012).
6. Y. Cotte, F. Toy, P. Jourdain, N. Pavillon, D. Boss, P. Magistretti, P. Marquet, and C. Depeursinge, "Marker-free phase nanoscopy," Nat. Photonics **7**, 113–117 (2013).
7. N. Destouches, C. A. Guérin, M. Lequime, and H. Giovaninni, "Determination of the phase of the diffracted field in the optical domain. application to the reconstruction of surface profiles," Opt. Commun. **198**, 233–239 (2001).
8. O. Haeberlé, K. Belkebir, H. Giovaninni, and A. Sentenac, "Tomographic diffractive microscopy: basics, techniques and perspectives," J. Mod. Opt. **57**, 686–699 (2010).
9. E. Mudry, P. C. Chaumet, K. Belkebir, G. Maire, and A. Sentenac, "Mirror-assisted tomographic diffractive microscopy with isotropic resolution," Opt. Lett. **35**, 1857–1859 (2010).
10. E. Mudry, E. L. Moal, P. Ferrand, P. C. Chaumet, and A. Sentenac, "Isotropic diffraction-limited focusing using a single objective lens," Phys. Rev. Lett. **105**, 203903 (2010).
11. S. W. Hell and E. H. K. Stelzer, "Fundamental improvement of resolution with a 4pi-confocal fluorescence microscope using two-photon excitation," Opt. Commun. **93**, 277–282 (1992).
12. V. Mico, Z. Zalevsky, P. Garcia-Martinez, and J. Garcia, "Synthetic aperture superresolution with multiple off-axis holograms," J. Opt. Soc. Am. A **23**, 3162–3170 (2006).
13. S. A. Alexandrov, T. R. Hillman, T. Gutzler, and D. D. Sampson, "Synthetic aperture Fourier holographic optical microscopy," Phys. Rev. Lett. **97**, 168102 (2006).
14. M. Sarmis, B. Simon, M. Debailleul, B. Colicchio, V. Georges, J.-J. Delaunay, and O. Haeberlé, "High resolution reflection tomographic diffractive microscopy," J. Mod. Opt. **57**, 740–745 (2010).
15. G. Maire, F. Drsek, J. Girard, H. Giovannini, A. Talneau, D. Konan, K. Belkebir, P. C. Chaumet, and A. Sentenac, "Experimental demonstration of quantitative imaging beyond Abbe's limit with optical diffraction tomography," Phys. Rev. Lett. **102**, 213905 (2009).
16. J. Girard, G. Maire, H. Giovannini, A. Talneau, K. Belkebir, P. C. Chaumet, and A. Sentenac, "Nanometric resolution using farfield optical tomographic microscopy in the multiple scattering regime," Phys. Rev. A **82**, 061801 (2010).
17. S. Arhab, G. Soriano, Y. Ruan, G. Maire, A. Talneau, D. Sentenac, P. Chaumet, K. Belkebir, and H. Giovannini, "Nanometric resolution with far-field optical profilometry," Phys. Rev. Lett. **111**, 053902 (2013).
18. Y. Ruan, P. Bon, E. Mudry, G. Maire, P. C. Chaumet, H. Giovannini, K. Belkebir, A. Talneau, B. Wattellier, S. Monneret, and A. Sentenac, "Tomographic diffractive microscopy with a wavefront sensor," Opt. Lett. **37**, 1631–1633 (2012).
19. M. Born and E. Wolf, *Principles of Optics* (Pergamon, 1959).
20. O. Haeberlé, A. Sentenac, and H. Giovannini, *An Introduction to Diffractive Tomographic Microscopy*, A. M. Vilas and J. D. Alvarez, eds., Modern Research and Educational Topics in Microscopy, Vol. **II** (Formatex, 2007).
21. K. Belkebir, P. C. Chaumet, and A. Sentenac, "Influence of multiple scattering on three-dimensional imaging with optical diffraction tomography," J. Opt. Soc. Am. A **23**, 586–595 (2006).
22. P. C. Chaumet and K. Belkebir, "Three-dimensional reconstruction from real data using a conjugate gradient-coupled dipole method," Inverse Probl. **25**, 024003 (2009).
23. P. C. Chaumet, A. Sentenac, and A. Rahmani, "Coupled dipole method for scatterers with large permittivity," Phys. Rev. E **70**, 036606 (2004).
24. E. Mudry, P. C. Chaumet, K. Belkebir, and A. Sentenac, "Electromagnetic wave imaging of three-dimensional targets using a hybrid iterative inversion method," Inverse Probl. **28**, 065007 (2012).
25. J. D. Jackson, *Classical Electrodynamics*, 2nd ed. (Wiley, 1975).
26. K. Belkebir, P. C. Chaumet, and A. Sentenac, "Superresolution in total internal reflection tomography," J. Opt. Soc. Am. A **22**, 1889–1897 (2005).
27. The experiment was automatized using the free software OpticsBenchUI.
28. G. Maire, J. Girard, F. Drsek, H. Giovannini, A. Talneau, K. Belkebir, P. C. Chaumet, and A. Sentenac, "Experimental inversion of optical diffraction tomography data with a nonlinear algorithm in the multiple scattering regime," J. Mod. Opt. **57**, 746–755 (2010).